ACS APPLIED MATERIALS & INTERFACES

Research Article

www.acsami.org

Formation of a Crack-Free, Hybrid Skin Layer with Tunable Surface Topography and Improved Gas Permeation Selectivity on Elastomers Using Gel–Liquid Infiltration Polymerization

Mengyuan Wang,[†,‡] Justin M. Gorham,[§] Jason P. Killgore,[∥] Maryam Omidvar,[⊥] Haiqing Lin,[⊥] Frank W. DelRio,[∥] Lewis M. Cox,[∥] Zheng Zhang,[#] and Yifu Ding*[,†,‡]

[†]Materials Science and Engineering Program, University of Colorado at Boulder, Boulder, Colorado 80309-0596, United States

[‡]Department of Mechanical Engineering, University of Colorado at Boulder, Boulder, Colorado 80309-0427, United States

[§]Materials Measurement Science Division, National Institute of Standards and Technology (NIST), Gaithersburg, Maryland 20899, United States

[∥]Applied Chemicals and Materials Division, National Institute of Standards and Technology (NIST), Boulder, Colorado 80305, United States

[⊥]Department of Chemical and Biological Engineering, University at Buffalo, The State University of New York, Buffalo, New York 14260, United States

[#]Center for Functional Nanomaterials, Brookhaven National Laboratory, Upton, New York 11973-5000, United States

Supporting Information

ABSTRACT: Surface modifications of elastomers and gels are crucial for emerging applications such as soft robotics and flexible electronics, in large part because they provide a platform to control wettability, adhesion, and permeability. Current surface modification methods via ultraviolet-ozone (UVO) and/or O_2 plasma, atomic layer deposition (ALD), plasmas deposition, and chemical treatment impart a dense polymer or inorganic layer on the surface that is brittle and easy to fracture at low strain levels. This paper presents a new method, based on gel–liquid infiltration polymerization, to form hybrid skin layers atop elastomers. The method is unique in that it allows for control of the skin layer topography, with tunable feature sizes and aspect ratios as high as 1.8 without fracture. Unlike previous techniques, the skin layer formed here dramatically improves the barrier properties of the elastomer, while preserving skin layer flexibility. Moreover, the method is versatile and likely applicable to most interfacial polymerization systems and network polymers on flat and patterned surfaces.

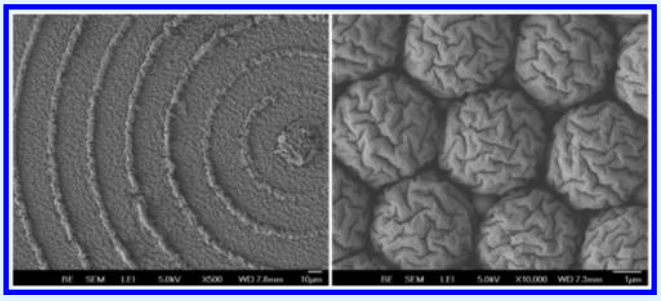

KEYWORDS: *surface modifications, gels and elastomers, skin layers, gas separation membranes, surface wrinkles*

INTRODUCTION

The flexibility of network polymers in their dry form (elastomer) and wet form (gels) has inspired applications in flexible electronics,[1,2] soft robotics,[3] optics,[4] sensors,[5] and microfluidics.[6] Often, surfaces of the elastomers and gels must be modified to meet the requirements of the desired applications, from solvent retention to harvest of new functionality. For example, a hydrophobic polymer layer has been coated onto a proton exchange membrane (PEM) using plasma treatment.[7] The coating layer cracked during the PEM hydration, but the crack openings progressively sealed during dehydration, which reduced the dehydration rate and improved the PEM performance at elevated temperatures. Besides continuous films, self-assembled colloidal particles can also be designed to form controlled cracks, useful for different applications.[8,9]

Surfaces of polydimethylsiloxane (PDMS), one of the most frequently studied elastomers, can be modified using a variety of methods. UVO and O_2 plasma treatments result in a SiO_x-like skin layer.[10] Under mechanical loading, such a stiff-on-compliant configuration leads to tunable surface features including microlenses and,[11] more commonly, surface wrinkles.[12,13] Using a periodic injection of tetraethyl orthosilicate (TEOS) and subsequent sol–gel deposition, a silica particle layer was deposited on the surface of PDMS particles, producing a series of unclonable microfingerprints.[14] ALD-based sequential infiltration synthesis (SIS) was applied to impart metal oxides such as AlO_x within the PDMS surface layer, which improved triboelectric generation performance.[15]

Received: June 27, 2017
Accepted: July 31, 2017
Published: July 31, 2017

DOI: 10.1021/acsami.7b09274
ACS Appl. Mater. Interfaces 2017, 9, 28100–28106

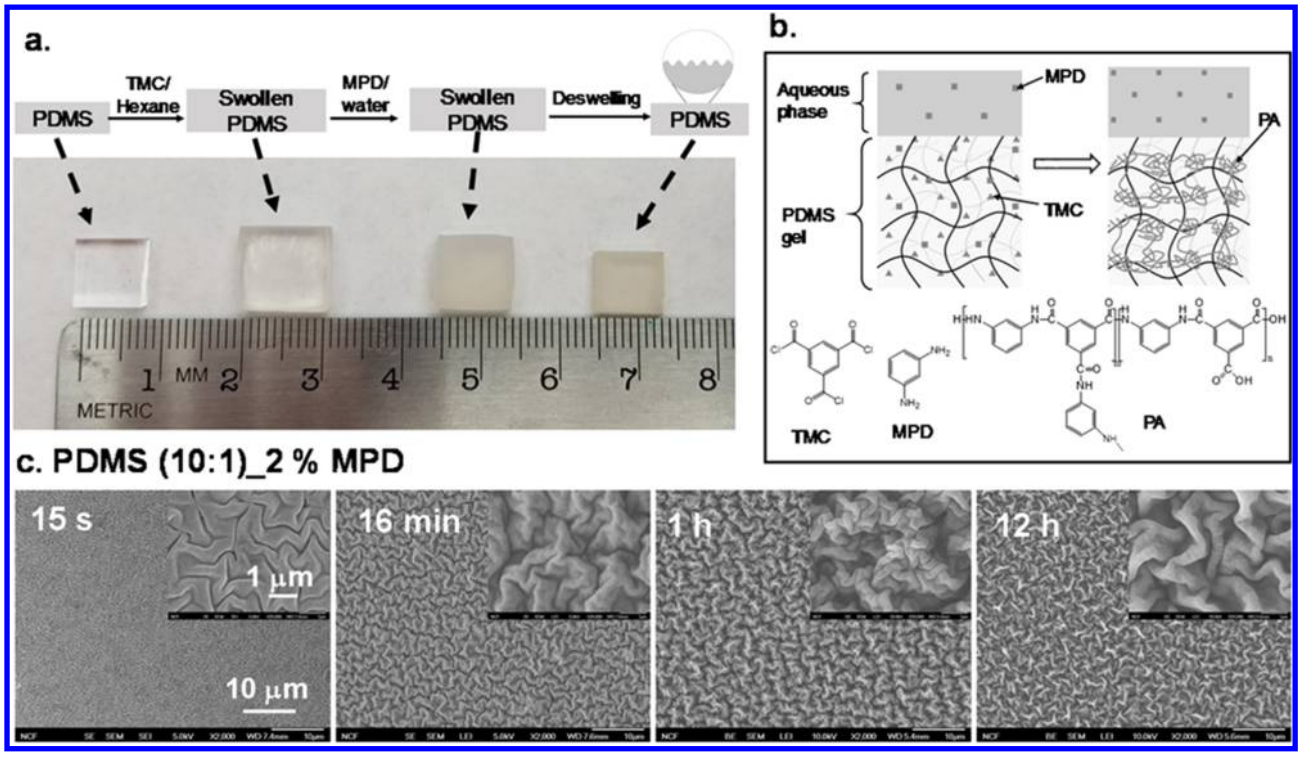

Figure 1. (a) Illustration of infiltration polymerization process, and photographs of PDMS samples at each step. (b) Mechanism of the PA/PDMS skin layer formation. (c) SEM images of the PDMS (10:1) surface after the infiltration polymerization process in 2% MPD solution for different durations as labeled. The scale bars in the main figure and the inset apply to all the images.

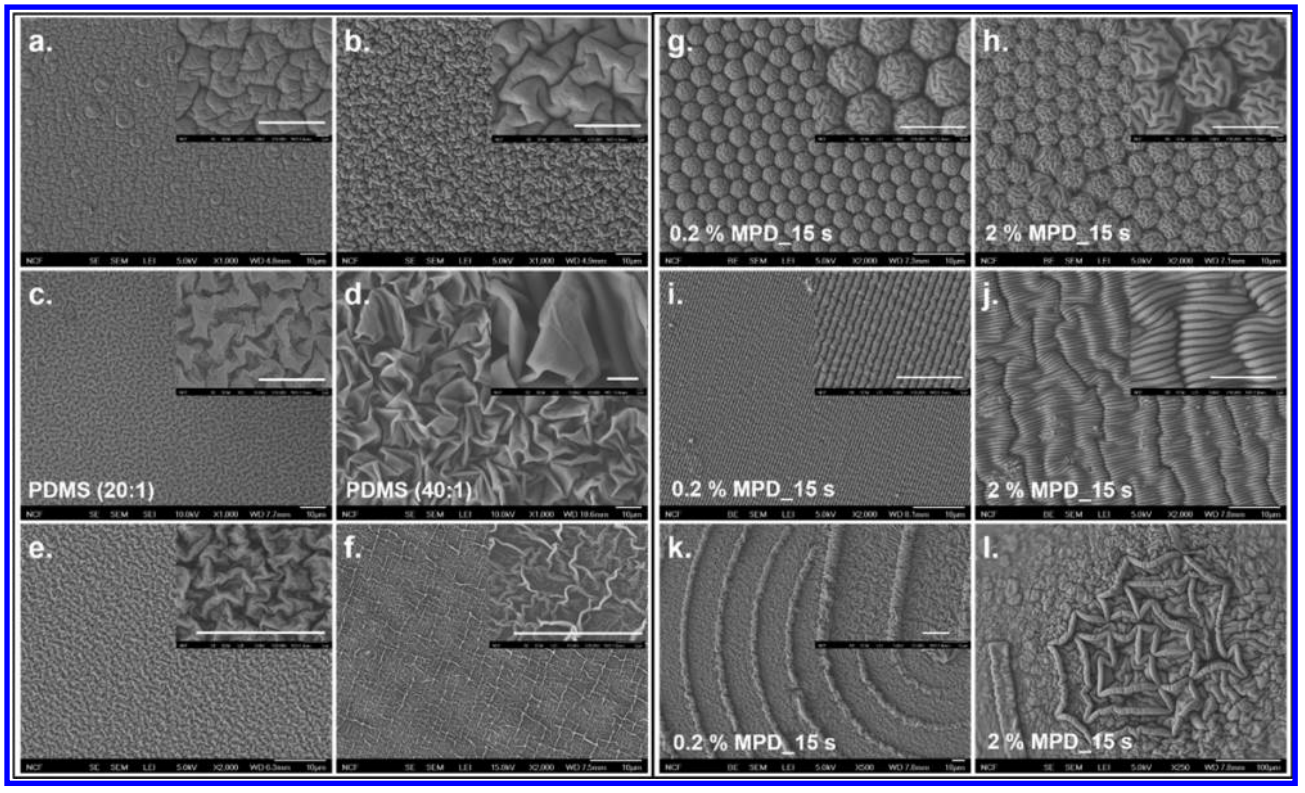

Figure 2. SEM images of the skin layers formed after 16 min reaction in (a–d) 2%, (e) 0.2%, and (f) 0.02% MPD solution: parts a and b are PDMS (10:1) with 3 and 10 min preswelling in TMC/hexane solution, respectively; parts c and d are PDMS (20:1) and PDMS (40:1) after equilibrium swelling in TMC/hexane solution; parts e and f are PDMS (10:1) with equilibrium swelling in TMC/hexane. Parts g–l are SEM images of the patterned PDMS (10:1) after reaction under conditions as labeled: (g, h) microlens, (i, j) line-and-space gratings, (k) concentric ring, and (l) "CU" lettering. The scale bars in the insets for parts a–j correspond to a length of 5 μm, and 10 μm in part k.

DOI: 10.1021/acsami.7b09274
ACS Appl. Mater. Interfaces 2017, 9, 28100–28106

However, the UVO-derived inorganic layers are brittle, while the SIS method is inefficient in terms of both throughput and chemical specificity.

Here, we report a simple and versatile method that can modify the surface of elastomers using gel−liquid infiltration polymerization (GLIP). Using PDMS as a model system, the process allowed formation of hybrid polyamide (PA)/PDMS skin layers, which sustained very large local strain without fracture, dramatically reduced the solvent/gas permeation, and improved gas selectivity.

RESULTS AND DISCUSSION

Figure 1a illustrates the GLIP process. A PDMS film, swollen with trimesoyl chloride (TMC)/hexane solution, was placed within an aqueous solution containing 1,3-phenylenediamine (MPD). Due to the asymmetry in solubility,[16,17] MPD diffused into the PDMS gel and polymerized with the TMC, forming a PA/PDMS skin layer (Figure 1b). We chose the MPD/TMC system because the reaction is fast (within seconds to minutes depending on monomer concentration), and self-limiting (i.e., the skin layer serves as a barrier for further monomer diffusion and thus limits the skin layer thickness).[18−20] As the hexane evaporated, the PDMS substrate compressed and wrinkled the skin layer (Figure 1a). The maximum strain loading (ε_m) occurred when the skin layer had negligible solvent content, $\varepsilon_m = (l_d - l_s)/l_s$, where l_d and l_s are the dimensions of the PDMS at swollen and dry states, correspondingly. For equilibrium swollen PDMS (10:1), ε_m = −31.7%, consistent with the literature report.[21]

Figure 1c shows the surface morphology of the PDMS (10:1) after reacting in 2% MPD solution for different durations (TMC concentration was fixed at 0.2% for all the samples). Topographic atomic force microscopy (AFM) images for all the samples are shown in Figures S1−S3, and geometry of the surface features is summarized in Table S1. The lateral feature size of the wrinkle-like structure increased from ≈0.6 μm to ≈2 μm as the reaction time increased from 15 s to 16 min, while the aspect ratio (height/bottom width) of these features was similar, ranging from 0.5 to 0.6. For samples with 1 and 2 h reaction, the surface topography became more hierarchical, showing a combination of small ridges (width ≈400−500 nm and aspect ratios ≈0.7−1.0) and larger features (width ≈2−2.5 μm). After 12 h, the small ridges become the dominant morphology with aspect ratio ≈1.0 (Figure 1c).

The skin layer morphology can be controlled by the process parameters, as collectively demonstrated in Figure 2. Instead of equilibrium swelling, PDMS (10:1) was swollen in a TMC/hexane solution for 3 and 10 min, to achieve ε_m = −10.7% and ε_m = −20.0%, correspondingly. After reacting in 2% MPD solution for 16 min, both samples displayed a creased skin layer with randomly oriented folds (Figure 2a,b), with 1−3 μm average distances between the neighboring folds. The folds of the sample with ε_m = −20.0% (0.7−1.5 μm) were deeper than the sample with ε_m = −10.7% (0.3−0.9 μm). Adjusting the cross-linking density of PDMS also leads to different degrees of swelling: for 20:1 and 40:1 curing ratios, ε_m increased to ≈−40.0% and ≈−58.5%. After 16 min in 2% MPD solution, the PDMS (20:1) sample displayed highly hierarchical surface structures (Figure 2c): deep wrinkles ≈2−3 μm wide and 0.7−1.6 μm deep, together with narrower (200−300 nm) and shallower (≈200 nm) wrinkles. For the PDMS (40:1) sample (Figure 2d), a ridge-like skin layer morphology with extremely high aspect ratio was observed: the width of the ridges was ≈2 μm, but the height was above the measurement limits of the AFM. From scanning electron microscopy (SEM) images, the aspect ratio of the ridges can be up to ≈1.8 (see Figure S4 and following discussion in SI).

Achieving high aspect ratio wrinkles and ridges using stiff-on-compliant configurations has been a challenge,[22−25] because the stiff layers typically have low fracture strain. Under uniaxial compressive loading, the stiff layers often crack because of the tensile loading at the perpendicular direction, which can be minimized using biaxial compression. Recently, using incremental release of large prestretch[26,27] or plastic deformation,[28] structures with aspect ratios as high as 1.5[24] and 2.0[22] were fabricated. The method presented here yielded tunable skin layer morphology from hierarchical wrinkles to folds/ridges. According to Cao et al.,[24] the aspect ratio of ridge-like structures is dictated by the prestrain (ε_{pre}) as $A_{ridge}/\lambda_{ridge} = 0.52\varepsilon_{pre} + 0.23$. With this relationship, the PDMS (10:1) and (20:1) systems should have ε_{pre} of 45% and 67%, corresponding to predicted values of $A_{ridge}/\lambda_{ridge}$ of 0.46 and 0.58. As listed in Table S1, the dominant wrinkle morphologies have aspect ratios ranging from 0.5 to 1.1 for the PDMS (10:1) and PDMS (20:1) systems, which are comparable with the predicted values. For the PDMS (40:1) system, ε_{pre} was ∼142%, corresponding to $A_{ridge}/\lambda_{ridge}$ = 0.98, which is lower than the experimental estimation (up to 1.8). The discrepancy between the predicted values and our experimental data is likely resulting from both the fact that our skin layer is not a homogeneous continuous film as used in the FEA modeling, and the uncertainty in defining λ_{ridge} for the less periodic structures such as the PDMS (40:1) system. Nevertheless, such rough skin layers have large true surface area (A_t), as listed in Table S1. Specifically, A_t approaches a maximum value of 214% and 277% of the projected area (A_0) for the PDMS (10:1) and PDMS (20:1) systems. A_t for PDMS (40:1) was not determined, as the surface roughness was beyond the measurement limit of the AFM.

In traditional interfacial polymerization of TMC/MPD, both thickness and morphology of the PA layer can be controlled by monomer concentration and reaction time.[16,29] PA thickness as low as 8 nm was achieved with low MPD concentration, which led to superior membrane performance.[20] This suggests that similar surface-layer control may be possible in GLIP. Figure 2e,f shows the skin layers formed on PDMS (10:1) after 16 min of reaction in 0.2% and 0.02% MPD solutions (samples with shorter reaction times are shown in Figure S3). For the 0.2% MPD systems, wrinkle-like structures were observed, with both the feature size and degree of hierarchy increasing with reaction time (Table S1). For the 0.02% MPD system, however, the skin layer appeared distinctively different from that for both the 2% and 0.2% MPD systems. Specifically, perpendicular ridges with widths increasing from ≈160 nm at 15 s to 430 nm at 16 min and aspect ratios increasing from 0.6 to 1.0 were observed. In this low concentration system, the shrinkage-induced compressive strain was apparently highly localized.

In addition to topographically reconfiguring flat surfaces, the GLIP method can also modify prepatterned PDMS surfaces, including microlenses (Figure 2g,h), line-and-space gratings (Figure 2i,j), concentric rings (Figure 2k), and custom "CU" lettering (Figure 2l). For a given surface pattern, higher MPD concentrations and/or longer reaction times led to the formation of a thicker or stiffer skin layer, and thus larger instability-derived features. Unlike flat surfaces, the symmetry of the prepatterns dictates the local strain state and thus the

DOI: 10.1021/acsami.7b09274
ACS Appl. Mater. Interfaces 2017, 9, 28100−28106

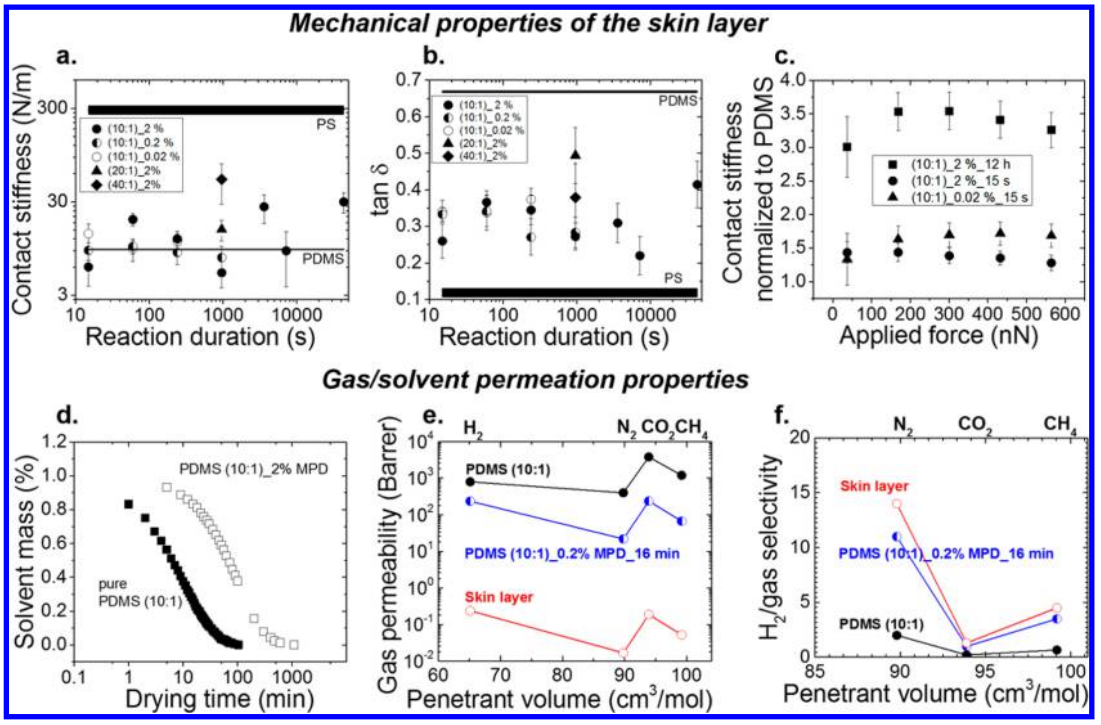

Figure 3. Parts a and b show the contact stiffness and loss tangent as a function of reaction duration. Horizontal bars represent properties of bulk references (PS and PDMS). Part c shows the contact stiffness of the modified surfaces, normalized by the value of bulk PDMS, as a function of applied force. (d) Solvent mass, normalized by the initial value, in the PDMS as a function of drying time for pure and modified PDMS. Comparison of (e) pure gas permeability and (f) H_2/gas selectivity in pure PDMS (data from ref 35) and PDMS (10:1) 0.2% MPD 16 min and the estimated PA-filled skin layer.

orientation of the wrinkles: randomly oriented short folds on a lens (Figure 2g,h), folds along grating lines (Figure 2i,j), and a combination of both in the concentric ring (wide trenches vs thin lines).

TMC/MPD-derived PA layers on traditional interfacially polymerized reverse osmosis (RO) membranes have a glass transition temperature, T_g, from 140 to 190 °C.[30] At room temperature, a dense PA layer is expected to be brittle, and will not survive the large-strain deformations observed in the ridges and folds. As such, the highly strained nature of the GLIP films indicates that the composition of the surface layer is not that of homogeneous PA, but something far more ductile. Consistently, from the top-down and cross-sectional SEM images (Figure S5), no clear signs of phase separation between the PA and PDMS were evident.

To determine the composition and morphology of the GLIP surface layer, a series of chemical and mechanical characterizations were performed. X-ray photoelectron spectroscopy (XPS) measurements revealed that the modified PDMS surfaces contained C, O, N, and Si, which consisted of 99% of the total elements detected (Figure S6 for the survey scan and Table S2 for the summary). All sample surfaces showed an appreciable amount of Si, which allows estimation of the C % and O % contributed from the PDMS. Accordingly, the atomic percentage of C, O, N from PA (and residual monomers) can be extracted (see SI for detailed discussion), which further allows estimation of the mass concentration of PDMS in the top 5−10 nm layer (Table S2). For the PDMS (10:1) 2% MPD system, the PDMS surface concentration decreased to 24.4% after only 15 s reaction, and reached 12.2% after 12 h. In contrast, for samples reacting in solutions with lower MPD concentrations, the PDMS concentration at the surface was high (70% to 80%) regardless of reaction time.

The O/N ratio of the PA provides a good estimation of the chemical composition of the PA: O/N = 1 for a fully cross-linked network, and O/N = 2 for linear chains.[20] For the 2% MPD system, the O/N ratio decreased from 4.1 (15 s), to 1.1 (16 min), to 0.7 for longer reaction times (Table S2), all of which is consistent with MPD/TMC-derived PA.[20,31] In contrast, for samples that reacted with lower MPD concentrations (0.2% and 0.02%), the O/N ratios were higher than 2, indicating an excess of hydrolyzed TMC or insufficient MPD infiltration. As base-to-cross-linker ratio increased from 10:1 to 20:1 to 40:1, after 16 min in 2% MPD solution, the O/N ratio of the PA-like materials increased from 1.1, to 6.7, to 38.7, suggesting an increase in the concentration of TMC-derivatives. Consequently, the PDMS concentration in the skin layer increased from 38.6%, to 45.5%, to 71.9%. Water contact angle (CA, Table S2) of the PDMS samples also provides rough estimation of the surface chemistry, although it is convoluted with the effect of surface topography. Nevertheless, it appears that CA decreases with an increase in N at. %, from ≈108.4° to 114.7° for the pure PDMS,[32,33] to ≈60.6° for 13 at. % N. The latter value was close to the CA of MPD/TMC-derived PA (≈51.2° to 60.6°).[20]

Whereas XPS and CA measurements are strongly surface-sensitive, they do not provide insight into the mechanics and morphology of the GLIP sample surface. Thus, contact resonance force microscopy (CR-FM) was used to probe the mechanical properties of the skin layers with high spatial resolution and sensitivity. In terms of elastic contact stiffness (Figure 3a), the samples are not readily differentiated from the PDMS reference until the longer reaction durations of the 2%

DOI: 10.1021/acsami.7b09274
ACS Appl. Mater. Interfaces 2017, 9, 28100−28106

MPD system are reached. For the 12 h reaction duration, the contact stiffness is ≈3 times greater than for the pure PDMS. Nonetheless, the highest contact stiffness observed on infiltration polymerized samples is still a factor of 10 lower than a PS reference, suggesting the surface is not glassy as for traditional interfacially polymerized PA. When comparing tan δ (Figure 3b), the damping of the modified PDMS surfaces is intermediate to both the PDMS and PS references, consistent with the model of a hybrid PA/PDMS material that is capable of extreme surface strain. Figure 3c plots the normalized (by pure PDMS) contact stiffness for several of the modified PDMS surfaces as a function of applied force. By controlling the applied force, we vary the depth of the stress field exerted beneath the AFM tip. If the hybrid layer were of similar or smaller dimensions than the stress field, a greater percentage of pure PDMS would enter the stress field as we press harder, resulting in a convergence (ratio = 1) of the infiltration polymerized properties and the bulk PDMS properties. For both 2% MPD samples, slight divergence of the normalized stiffness ratio from 1 is observed. Only the 0.02% MPD at 15 s sample shows convergence toward the PDMS value; however, the trend is weak and could originate from epistemic uncertainties in the analysis. From Hertzian contact mechanics, we predict a stress field dominated by the top 30−50 nm of the sample for the lowest applied force and 100−150 nm for the highest applied force, suggesting a hybrid layer thickness of >100 nm. Beyond the average mechanical properties of the surface layer, CR-FM also provides insight into the mixing length scale of the PA/PDMS hybrid. When considering measurements obtained at all locations in the GLIP material, no data points exhibited a nanomechanical signature (i.e., a combination of stiffness and tan δ) equivalent to either the PDMS or PS references. Thus, the hybridization occurs at length scales smaller than the contact radius (i.e., <20 nm).

The presence of a denser skin layer with large A_t would significantly improve the barrier properties of the PDMS for solvent permeation.[34] For example, Figure 3d shows that the hexane loss rate of GLIP PDMS (10:1, 2% MPD, 16 min) ($t_{1/2}$ ≈ 68.5 min) is ≈10 times slower than that of the pure PDMS ($t_{1/2}$ ≈ 6.2 min) with identical geometry. The skin layer comprises highly cross-linked PA, resulting in the barrier properties.

We further demonstrate the barrier properties of the skin layer using gas permeation through the GLIP PDMS (10:1, 2% MPD, 16 min). The GLIP PDMS showed significantly lower gas (H_2, N_2, CH_4, and CO_2) permeability (Figure 3e) than pure PDMS,[35] confirming the impact of the skin layer with highly cross-linked rigid networks and thus lower gas permeability. On the other hand, the skin layer significantly increased the H_2/gas selectivity (Figure 3f) because of the enhanced size-sieving ability and diffusive selectivity in the rigid skin layer. For example, H_2/N_2 selectivity in the GLIP PDMS is 11, which is significantly higher than that in pure PDMS (=2.0) or the Knudsen selectivity (=3.7). Using a resistance-in-series model[36] (see SI for details), the estimated gas permeability and H_2/gas selectivity in the skin layer is presented in Figure 3f. The GLIP skin layer has almost 4 orders of magnitude lower permeability and dramatically higher H_2/gas selectivity than the underlying PDMS. Although further studies will be needed to thoroughly quantify the gas transport properties of the skin layer, the demonstration clearly reveals that the presence of the skin layer, even modified with 0.2% MPD concentration, can significantly reduce the permeation and enhance the gas selectivity.

CONCLUSION

In conclusion, we report a versatile method to modify the surface of PDMS, by using gel−liquid infiltration polymerization. Because of both the self-limiting nature of the TMC/MPD reaction and the network constraints for nanogel diffusion, PA formed only near the PDMS surface, yielding a crack-free hybrid skin layer. The skin layers have low solvent solubility and are stiffer than the bulk PDMS, which leads to the formation of a series of hierarchical surface features on the dried PDMS with aspect ratio as high as 1.8 without fracture. We demonstrated that the morphology and properties of the skin layers can be controlled by adjusting both the process conditions and substrate topography, and that the skin layers significantly reduce the solvent/gas permeation and improve the gas selectivity. Different from the reactive infusion process where a reactive silane diffused and covalently bound to the network,[37] the infiltrated polyamide is physically fused with the PDMS network within the skin layer. Thus, the GLIP process is extremely versatile: the infiltrated polymers can be selected from a broad range of interfacial polymerization systems,[38] and the substrates can be any polymer networks. Recently, studies have shown that imparting surface topography on separation membranes can enhance separation performances, from increasing permeation[39] to improving antifouling performances due to the topography-enhanced back diffusion.[40,41] We envision that the approach reported here can be used to improve different separation applications from gas separation to pervaporation.

EXPERIMENTAL SECTION

Infiltration Polymerization Process. PDMS films (Sylgard 184, Dow Corning) with base-to-curing-agent ratio of 10:1, 20:1, and 40:1 were cured at 80 °C for 2 h, and were cut into 8 mm × 8 mm pieces (≈2 mm thick) for the subsequent experiments. PDMS samples were swollen in a hexane (Fisher Scientific) solution containing 0.2% TMC (99%) for different durations, followed by reaction in an aqueous solution containing MPD (0.02%, 0.2%, or 2%), 2% triethylamine (TEA), and 4% (1*S*)-(+)-10-camphor-10-sulfonic acid (CSA) for different durations.[19,42] MPD, TEA, and CSA were purchased from MilliporeSigma, and used as received, and all concentrations were mass percentages unless otherwise noted. After the reaction, the PDMS samples were rinsed with DI water and dried under a chemical hood for 24 h. In addition to the flat surface, PDMS (10:1) with three types of surface patterns were examined: line-and-space gratings, concentric rings, and microlenses. The gratings and concentric rings were replicated by curing PDMS onto Si templates, which were fabricated with standard photolithography.[43,44] The PDMS microlenses were replicated from PS templates, which were fabricated using a breath-figure-templated self-assembly (BFTA) method.[45]

Characterization of Skin Layer. Field emission SEM (JEOL JSM-7401F) was used to characterize both the surface and cross sections of the modified PDMS. All the samples were coated with a ≈5 nm gold layer before SEM measurements. Quantitative analysis of the surface topography was carried out with an AFM (DI 3100, Bruker). For each sample, measurements at three randomly selected locations across the surface were carried out. A second AFM (Cypher, Asylum Research) was used to perform viscoelastic nanomechanical characterization of the sample surface with CR-FM,[46] applying a 3 N/m cantilever with a specially fabricated hemispherical tip of 60 nm nominal radius (HSC 60, Team Nanotec). The third eigenmode free resonance frequencies and quality factors of the cantilever were compared to corresponding values of the cantilever in contact with the sample to determine the effective loss tangent and contact stiffness of the sample surface.[46,47] At least 15 locations on each sample were probed with an applied force of 35 nN ± 5 nN. A subset of samples

DOI: 10.1021/acsami.7b09274
ACS Appl. Mater. Interfaces 2017, 9, 28100−28106

representing expected property extremes was characterized at a range of forces from 35 nN ± 3.5 nN to 565 nN ± 57 nN.

Surface elemental analyses were carried out using XPS with an Axis Ultra DLD imaging spectrophotometer (Kratos Analytical) and monochromatic Al Kα X-rays (8 mA; 13 kV). Emitted photoelectrons were collected along the surface normal over a field of view defined by a hybrid lens and a slot aperture (over 90% of signal from a 0.94 mm × 2.25 mm area),[48] with the exception of the native PDMS films which were collected using a FOV1 lens and a 110 μm aperture. For each specimen, high resolution spectra were acquired for O 1s, N 1s, C 1s, Si 2p, Cl 2p, and S 2p. All spectra were energy corrected by adjusting the Si 2p peak position to 102.1 eV, a value comparable with literature references for PDMS.[49] All spectra were fit with Shirley backgrounds, and peak areas were corrected using elemental relative sensitivity factors from the manufacturer. All values reported are the average value and standard deviation from 4 measurements at spots separated by 1−2 mm.

Water CA measurements were obtained with a custom-built image system (Fastcam SA4, Photron), with a 2 μL DI-water droplet. For each sample, at least three repeated measurements were carried out, and the average values are reported here. Pure gas permeability of H_2, N_2, CH_4, and CO_2 in PDMS (10:1) in 0.2% MPD for a 16 min sample was determined using a constant-volume and variable-pressure apparatus at 35 °C.[50,51] The PDMS films used have a thickness of ≈100 μm and an active area of 0.37 cm^2. The feed pressure was varied at 50 and 100 psig, while the downstream was kept under vacuum, and the steady-state rate of pressure increase in the fixed downstream volume was recorded and used to calculate gas permeability. Permeability of the film to gas component has units of Barrer (1 Barrer = 1 × 10^{-10} cm^3 (STP) cm cm^{-2} s^{-1} cm Hg^{-1}).

■ ASSOCIATED CONTENT

Supporting Information

The Supporting Information is available free of charge on the ACS Publications website at DOI: 10.1021/acsami.7b09274.

Additional experimental details and analysis, including conditions for all the samples prepared, topographic AFM images of the surface and corresponding analysis, cross-sectional SEM of the skin layer, XPS analysis (survey scans and detailed elemental analysis), and analysis of gas permeation (PDF)

■ AUTHOR INFORMATION

Corresponding Author

*E-mail: yifu.ding@colorado.edu.

ORCID

Haiqing Lin: 0000-0001-8042-154X

Lewis M. Cox: 0000-0002-5830-3819

Yifu Ding: 0000-0001-7779-7781

Author Contributions

The manuscript was written through contributions of all authors. All authors have given approval to the final version of the manuscript.

Notes

The authors declare no competing financial interest.

■ ACKNOWLEDGMENTS

M.W. and Y.D. acknowledge the funding support from the NSF under Grant CMMI-1233626 and CBET-1264276. Publication of NIST, an agency of the US government, not subject to copyright. Certain commercial equipment, instruments, or materials are identified in this paper to specify the experimental procedure adequately. Such identification does not imply recommendation or endorsement by NIST, nor does it imply that the materials or equipment identified are necessarily the best available for the purpose.

■ REFERENCES

(1) Lin, S. T.; Yuk, H.; Zhang, T.; Parada, G. A.; Koo, H.; Yu, C. J.; Zhao, X. H. Stretchable Hydrogel Electronics and Devices. *Adv. Mater.* **2016**, *28* (22), 4497−4505.

(2) Liu, Y. H.; Norton, J. J. S.; Qazi, R.; Zou, Z. N.; Ammann, K. R.; Liu, H.; Yan, L. Q.; Tran, P. L.; Jang, K. I.; Lee, J. W.; Zhang, D.; Kilian, K. A.; Jung, S. H.; Bretl, T.; Xiao, J. L.; Slepian, M. J.; Huang, Y. G.; Jeong, J. W.; Rogers, J. A. Epidermal Mechano-Acoustic Sensing Electronics for Cardiovascular Diagnostics and Human-Machine Interfaces. *Sci. Adv.* **2016**, *2* (11), 1601185.

(3) Yuk, H.; Lin, S. T.; Ma, C.; Takaffoli, M.; Fang, N. X.; Zhao, X. H. Hydraulic Hydrogel Actuators and Robots Optically and Sonically Camouflaged in Water. *Nat. Commun.* **2017**, *8*, 14230.

(4) Guo, J. J.; Liu, X. Y.; Jiang, N.; Yetisen, A. K.; Yuk, H.; Yang, C. X.; Khademhosseini, A.; Zhao, X. H.; Yun, S. H. Highly Stretchable, Strain Sensing Hydrogel Optical Fibers. *Adv. Mater.* **2016**, *28* (46), 10244−10249.

(5) Sohn, K. S.; Timilsina, S.; Singh, S. P.; Lee, J. W.; Kim, J. S. A Mechanoluminescent ZnS:Cu/Rhodamine/SiO2/PDMS and Piezoresistive CNT/PDMS Hybrid Sensor: Red-Light Emission and a Standardized Strain Quantification. *ACS Appl. Mater. Interfaces* **2016**, *8* (50), 34777−34783.

(6) Yuk, H.; Zhang, T.; Parada, G. A.; Liu, X. Y.; Zhao, X. H. Skin-Inspired Hydrogel-Elastomer Hybrids with Robust Interfaces and Functional Microstructures. *Nat. Commun.* **2016**, *7*, 12028.

(7) Park, C. H.; Lee, S. Y.; Hwang, D. S.; Shin, D. W.; Cho, D. H.; Lee, K. H.; Kim, T. W.; Lee, M.; Kim, D. S.; Doherty, C. M.; Thornton, A. W.; Hill, A. J.; Guiver, M. D.; Lee, Y. M. Nanocrack-Regulated Self-Humidifying Membranes. *Nature* **2016**, *532* (7600), 480−483.

(8) Han, W.; Li, B.; Lin, Z. Q. Drying-Mediated Assembly of Colloidal Nanoparticles into Large-Scale Microchannels. *ACS Nano* **2013**, *7* (7), 6079−6085.

(9) Li, B.; Jiang, B. B.; Han, W.; He, M.; Li, X.; Wang, W.; Hong, S. W.; Byun, M.; Lin, S. L.; Lin, Z. Q. Harnessing Colloidal Crack Formation by Flow-Enabled Self-Assembly. *Angew. Chem., Int. Ed.* **2017**, *56* (16), 4554−4559.

(10) Li, C. Y.; Liao, Y. C. Adhesive Stretchable Printed Conductive Thin Film Patterns on PDMS Surface with an Atmospheric Plasma Treatment. *ACS Appl. Mater. Interfaces* **2016**, *8* (18), 11868−11874.

(11) Chan, E. P.; Crosby, A. J. Fabricating Microlens Arrays by Surface Wrinkling. *Adv. Mater.* **2006**, *18* (24), 3238−3242.

(12) Chiche, A.; Stafford, C. M.; Cabral, J. T. Complex Micropatterning of Periodic Structures on Elastomeric Surfaces. *Soft Matter* **2008**, *4* (12), 2360−2364.

(13) Efimenko, K.; Rackaitis, M.; Manias, E.; Vaziri, A.; Mahadevan, L.; Genzer, J. Nested Self-Similar Wrinkling Patterns in Skins. *Nat. Mater.* **2005**, *4* (4), 293−297.

(14) Bae, H. J.; Bae, S.; Park, C.; Han, S.; Kim, J.; Kim, L. N.; Kim, K.; Song, S. H.; Park, W.; Kwon, S. Biomimetic Microfingerprints for Anti-Counterfeiting Strategies. *Adv. Mater.* **2015**, *27* (12), 2083−2089.

(15) Yu, Y. H.; Li, Z. D.; Wang, Y. M.; Gong, S. Q.; Wang, X. D. Sequential Infiltration Synthesis of Doped Polymer Films with Tunable Electrical Properties for Efficient Triboelectric Nanogenerator Development. *Adv. Mater.* **2015**, *27* (33), 4938−4944.

(16) Freger, V. Kinetics of Film Formation by Interfacial Polycondensation. *Langmuir* **2005**, *21* (5), 1884−1894.

(17) Freger, V.; Srebnik, S. Mathematical Model of Charge and Density Distributions in Interfacial Polymerization of Thin Films. *J. Appl. Polym. Sci.* **2003**, *88* (5), 1162−1169.

(18) Maruf, S. H.; Greenberg, A. R.; Ding, Y. F. Influence of Substrate Processing and Interfacial Polymerization Conditions on the Surface Topography and Permselective Properties of Surface-Patterned Thin-Film Composite Membranes. *J. Membr. Sci.* **2016**, *512*, 50−60.

DOI: 10.1021/acsami.7b09274
ACS Appl. Mater. Interfaces 2017, 9, 28100−28106

(19) Maruf, S. H.; Greenberg, A. R.; Pellegrino, J.; Ding, Y. Fabrication and Characterization of a Surface-Patterned Thin Film Composite Membrane. *J. Membr. Sci.* **2014**, *452*, 11−19.
(20) Karan, S.; Jiang, Z. W.; Livingston, A. G. Sub-10 nm Polyamide Nanofilms with Ultrafast Solvent Transport for Molecular Separation. *Science* **2015**, *348* (6241), 1347−1351.
(21) Lee, J. N.; Park, C.; Whitesides, G. M. Solvent Compatibility of Poly(dimethylsiloxane)-Based Microfluidic Devices. *Anal. Chem.* **2003**, *75* (23), 6544−6554.
(22) Ahmed, S. F.; Rho, G. H.; Lee, K. R.; Vaziri, A.; Moon, M. W. High Aspect Ratio Wrinkles on A Soft Polymer. *Soft Matter* **2010**, *6* (22), 5709−5714.
(23) Chen, Y.-C.; Wang, Y.; McCarthy, T. J.; Crosby, A. J. Achieving High Aspect Ratio Wrinkles by Modifying Material Network Stress. *Soft Matter* **2017**, *13* (22), 4142−4147.
(24) Cao, C. Y.; Chan, H. F.; Zang, J. F.; Leong, K. W.; Zhao, X. H. Harnessing Localized Ridges for High-Aspect-Ratio Hierarchical Patterns with Dynamic Tunability and Multifunctionality. *Adv. Mater.* **2014**, *26* (11), 1763−1770.
(25) Li, J. J.; An, Y. H.; Huang, R.; Jiang, H. Q.; Xie, T. Unique Aspects of a Shape Memory Polymer As the Substrate for Surface Wrinkling. *ACS Appl. Mater. Interfaces* **2012**, *4* (2), 598−603.
(26) Takei, A.; Jin, L. H.; Hutchinson, J. W.; Fujita, H. Ridge Localizations and Networks in Thin Films Compressed by the Incremental Release of a Large Equi-biaxial Pre-stretch in the Substrate. *Adv. Mater.* **2014**, *26* (24), 4061−4067.
(27) Chen, Y. C.; Crosby, A. J. High Aspect Ratio Wrinkles via Substrate Prestretch. *Adv. Mater.* **2014**, *26* (32), 5626−5631.
(28) Takei, A.; Jin, L. H.; Fujita, H.; et al. High-Aspect-Ratio Ridge Structures Induced by Plastic Deformation as a Novel Microfabrication Technique. *ACS Appl. Mater. Interfaces* **2016**, *8* (36), 24230−24237.
(29) Freger, V. Swelling and Morphology of the Skin Layer of Polyamide Composite Membranes: An Atomic Force Microscopy Study. *Environ. Sci. Technol.* **2004**, *38* (11), 3168−3175.
(30) Maruf, S. H.; Ahn, D. U.; Greenberg, A. R.; Ding, Y. F. Glass Transition Behaviors of Interfacially Polymerized Polyamide Barrier Layers on Thin Film Composite Membranes via Nano-Thermal Analysis. *Polymer* **2011**, *52* (12), 2643−2649.
(31) Khorshidi, B.; Thundat, T.; Fleck, B. A.; Sadrzadeh, M. Thin Film Composite Polyamide Membranes: Parametric Study on the Influence of Synthesis Conditions. *RSC Adv.* **2015**, *5* (68), 54985−54997.
(32) Lawton, R. A.; Price, C. R.; Runge, A. F.; Doherty, W. J.; Saavedra, S. S. Air Plasma Treatment of Submicron Thick PDMS Polymer Films: Effect of Oxidation Time and Storage Conditions. *Colloids Surf., A* **2005**, *253* (1−3), 213−215.
(33) Jin, M. H.; Feng, X. J.; Xi, J. M.; Zhai, J.; Cho, K. W.; Feng, L.; Jiang, L. Super-Hydrophobic PDMS Surface with Ultra-Low Adhesive Force. *Macromol. Rapid Commun.* **2005**, *26* (22), 1805−1809.
(34) Nadermann, N. K.; Chan, E. P.; Stafford, C. M. Bilayer Mass Transport Model for Determining Swelling and Diffusion in Coated, Ultrathin Membranes. *ACS Appl. Mater. Interfaces* **2015**, *7* (6), 3492−3502.
(35) Merkel, T. C.; Bondar, V. I.; Nagai, K.; Freeman, B. D.; Pinnau, I. Gas Sorption, Diffusion, and Permeation in Poly(dimethylsiloxane). *J. Polym. Sci., Part B: Polym. Phys.* **2000**, *38*, 415−434.
(36) Lin, H.; Thompson, S. M.; Serbanescu-Martin, A.; Wijmans, H. G.; Amo, K. D.; Lokhandwala, K.; Merkel, T. C. Dehydration of Natural Gas Using Membranes. Part I: Composite Membranes. *J. Membr. Sci.* **2012**, *413*−*414*, 70−81.
(37) Li, Y.; Peterson, J. J.; Jhaveri, S. B.; Carter, K. R. Patterned Polymer Films via Reactive Silane Infusion-Induced Wrinkling. *Langmuir* **2013**, *29* (14), 4632−4639.
(38) Raaijmakers, M. J. T.; Benes, N. E. Current Trends in Interfacial Polymerization Chemistry. *Prog. Polym. Sci.* **2016**, *63*, 86−142.
(39) Peters, A. M.; Lammertink, R. G. H.; Wessling, M. Comparing Flat and Micro-Patterned Surfaces: Gas Permeation and Tensile Stress Measurements. *J. Membr. Sci.* **2008**, *320* (1−2), 173−178.
(40) Ding, Y.; Maruf, S.; Aghajani, M.; Greenberg, A. R. Surface Patterning of Polymeric Membranes and Its Effect on Antifouling Characteristics. *Sep. Sci. Technol.* **2017**, *52* (2), 240−257.
(41) Choi, W.; Chan, E. P.; Park, J. H.; Ahn, W. G.; Jung, H. W.; Hong, S.; Lee, J. S.; Han, J. Y.; Park, S.; Ko, D. H.; Lee, J. H. Nanoscale Pillar-Enhanced Tribological Surfaces as Antifouling Membranes. *ACS Appl. Mater. Interfaces* **2016**, *8* (45), 31433−31441.
(42) Ghosh, A. K.; Jeong, B. H.; Huang, X. F.; Hoek, E. M. V. Impacts of Reaction and Curing Conditions on Polyamide Composite Reverse Osmosis Membrane Properties. *J. Membr. Sci.* **2008**, *311* (1−2), 34−45.
(43) Zhang, Z.; Hilton, G. C.; Yang, R. G.; Ding, Y. F. Capillary Rupture of Suspended Polymer Concentric Rings. *Soft Matter* **2015**, *11* (37), 7264−7269.
(44) Zhang, Z.; Ahn, D. U.; Ding, Y. Instabilities of PS/PMMA Bilayer Patterns with a Corrugated Surface and Interface. *Macromolecules* **2012**, *45* (4), 1972−1981.
(45) Maniglio, D.; Ding, Y.; Wang, L.; Migliaresi, C. One-step Process to Create Porous Structures in Cross-Linked Polymer Films via Breath-Figure Formations during In Situ Cross-Linking Reactions. *Polymer* **2011**, *52* (22), 5102−5106.
(46) Hurley, D. C.; Campbell, S. E.; Killgore, J. P.; Cox, L. M.; Ding, Y. Measurement of Viscoelastic Loss Tangent with Contact Resonance Modes of Atomic Force Microscopy. *Macromolecules* **2013**, *46* (23), 9396−9402.
(47) Killgore, J. P.; Yablon, D. G.; Tsou, A. H.; Gannepalli, A.; Yuya, P. A.; Turner, J. A.; Proksch, R.; Hurley, D. C. Viscoelastic Property Mapping with Contact Resonance Force Microscopy. *Langmuir* **2011**, *27* (23), 13983−13987.
(48) Barron, S. C.; Gorham, J. M.; Patel, M. P.; Green, M. L. High-Throughput Measurements of Thermochromic Behavior in V1−xNbxO2Combinatorial Thin Film Libraries. *ACS Comb. Sci.* **2014**, *16* (10), 526−534.
(49) Naumkin, A. V.; Kraut-Vass, A.; Gaarenstroom, S. W.; Powell, C. J. *NIST X-ray Photoelectron Spectroscopy Database*; NIST/Department of Commerce, 2000; Vol. NIST SRD 20, V4.1; https://srdata.nist.gov/xps/Default.aspx.
(50) Lin, H.; Freeman, B. D. Permeation and Diffusion. In *Handbook of Materials Measurement Methods*; Czichos, H., Smith, L. E., Saito, T., Eds.; Springer, 2006; pp 371−387.
(51) Yavari, M.; Maruf, S. H.; Ding, Y. F.; Lin, H. Physical Aging of Glassy Perfluoropolymers in Thin Film Composite Membranes. Part II. Glass Transition Temperature and the Free Volume Model. *J. Membr. Sci.* **2017**, *525*, 399−408.

DOI: 10.1021/acsami.7b09274
ACS Appl. Mater. Interfaces 2017, 9, 28100−28106